

# Structure of the Liquid–Vacuum Interface of Room-Temperature Ionic Liquids: A Molecular Dynamics Study

Tianying Yan,<sup>†,‡</sup> Shu Li,<sup>†</sup> Wei Jiang,<sup>§</sup> Xueping Gao,<sup>†</sup> Bing Xiang,<sup>‡</sup> and Gregory A. Voth<sup>\*,§</sup>

*Institute of New Energy Material Chemistry and Department of Material Chemistry, Nankai University, Tianjin 300071, China, Institute of Scientific Computing, Nankai University, Tianjin 300071, China, and Center for Biophysical Modeling and Simulation and Department of Chemistry, University of Utah, Salt Lake City, Utah 84112-0850*

*Received: October 14, 2005; In Final Form: November 19, 2005*

Molecular dynamics simulations for the liquid–vacuum interface of the ionic liquid 1-ethyl-3-methylimidazolium nitrate (EMIM<sup>+</sup>/NO<sub>3</sub><sup>−</sup>) were performed for both electronically polarizable and nonpolarizable potential energy surfaces. The interfacial structural properties, such as the oscillation in the number density profile, the orientational ordering, and the local clustering in the interfacial region, were calculated. The simulations with both the polarizable and nonpolarizable model demonstrate the existence of an inhomogeneous interfacial structure normal to the surface layer. It was found for both models that the ethyl tail group on EMIM<sup>+</sup> is likely to protrude outward from the surface. In the outmost surface layer, the cation is likely to lie on the surface with the imidazolium ring parallel to the interface, while there is a second region with enhanced density from that in the bulk where the cation preferably slants with the imidazolium ring tending to be perpendicular to the surface. The results also reveal that the electronic polarization effect is important for the ionic liquid interface. It is found that the cation is likely to be segregated at the ionic liquid surface for the polarizable model, while for the nonpolarizable model, the anion is found to be more likely to exhibit such behavior. The surface tension of the polarizable model (58.5 ± 0.5 mN/m) is much smaller than that of the nonpolarizable model (82.7 ± 0.6 mN/m), in better agreement with extrapolated experimental measurements on similar ionic liquid systems.

## I. Introduction

Room-temperature molten salts (RTMS), or ionic liquids (ILs), have prompted a significant amount of research in recent years. Like inorganic molten salts, ILs are composed solely of ions, but in contrast, their melting point is often less than 100 °C.<sup>1</sup> Most ILs of recent interest are based on nitrogen-rich alkyl-substituted heterocyclic cations, accompanied by different inorganic anions. ILs provide promising media for certain organic reactions, especially as solvents for transition metal catalysis. They can dissolve catalysts at high concentrations and form biphasic systems with numerous organic reactants and products. This makes it easy to extract products and recover homogeneous catalysts in multiphase reactions. Several publications to date show that switching from a normal organic solvent to an ionic liquid can lead to novel and unusual chemical reactivity. This opens up a wide field for future investigations into this new class of media.<sup>1,2</sup> Despite the current level of research activity, many of the properties of ILs remain to be elucidated.<sup>3</sup>

Recently, the structure of the gas–liquid and liquid–liquid interface of ionic liquids has been investigated computationally<sup>4,5</sup> and experimentally.<sup>6–17</sup> Most of these studies focus on ILs having an imidazolium ring with different attached alkyl chains. The first molecular dynamics (MD) simulation study of an ionic

liquid interface was performed by Lynden-Bell on 1,3-dimethylimidazolium chloride (DMIM<sup>+</sup>/Cl<sup>−</sup>),<sup>4</sup> in which it was found that the 2-fold rotation symmetry axis of the imidazolium ring is perpendicular to the surface normal with a methyl side group protruding from the surface. Also, there is a region of enhanced number density, in which the vertical alignment of the molecular planes allowed the cations to pack more closely. As the temperature was lowered, the degree of alignment increased slightly.

Watson and co-workers performed the first direct recoil spectrometry (DRS)<sup>6</sup> to investigate the molecular composition and orientation at the surface of the 1-butyl-3-methylimidazolium hexafluorophosphate (BMIM<sup>+</sup>/PF<sub>6</sub><sup>−</sup>) system. They found that the number of cations and anions is equal at the surface, and on average, the cations lie normal to the liquid surface while the C2 site (see Figure 1) points out toward the gas phase. Bowers and co-worker used neutron reflectometry (NR) to probe the interfacial structure of the ionic liquids 1-butyl-3-methylimidazolium tetrafluoroborate (BMIM<sup>+</sup>/BF<sub>4</sub><sup>−</sup>) and 1-octyl-3-methylimidazolium hexafluorophosphate (OMIM<sup>+</sup>/PF<sub>6</sub><sup>−</sup>).<sup>13</sup> Their results suggest that the cationic headgroups and anions are segregated from the alkyl-rich region and with a lamellar structure that exists at least two tiers of alkyl groups. A density oscillation near the surface is also evident from this study. Baldelli and co-workers performed sum frequency generation (SFG) spectroscopy on the 1-butyl-3-methylimidazolium bisperfluoroalkylimides (BMIM<sup>+</sup>/imide<sup>−</sup>) ionic liquid, and their study indicated that the butyl group chains are protruding out of the interface into the vacuum, with the charged imidazolium ring lying parallel to the surface.<sup>10,11</sup> These

\* To whom correspondence should be addressed. E-mail: voth@chem.utah.edu.

<sup>†</sup> Institute of New Energy Material Chemistry and Department of Material Chemistry, Nankai University.

<sup>‡</sup> Institute of Scientific Computing, Nankai University.

<sup>§</sup> University of Utah.

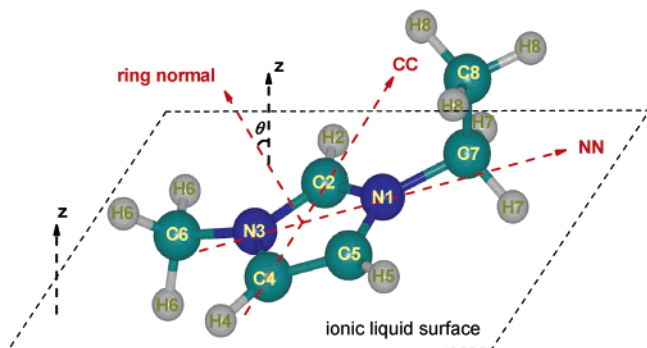


**Figure 1.** Definition of the direction vectors of the EMIM<sup>+</sup> cation in this study. The imidazolium ring normal direction is defined by the cross product of the NN vector (from N3 to N1) and the CC vector (from C4 to C2). The surface normal direction is denoted by  $z$ , and the angle,  $\theta$ , between a given direction vector and  $z$  is recorded during the MD simulation.

researchers also suggest that the cation is likely to be segregated on the surface because there are no detectable SFG signals for the anion, and also because the cation has a greater polarizability.<sup>10</sup> Deutsch and co-workers performed X-ray reflectivity (XR) on BMIM<sup>+</sup>/PF<sub>6</sub><sup>−</sup> and BMIM<sup>+</sup>/BF<sub>4</sub><sup>−</sup>,<sup>16</sup> and their study revealed that a layer of enhanced density exists at the surface layer. These authors also suggested two possible arrangements of the ions at the surface, which are different from those of the other studies.

Interfacial structure influences many important properties of macroscopic matter, such as the solubility, the extent of liquid supercooling, the vapor pressure, etc. In addition, many important properties of liquids depend on the characteristics and structure of the liquid–vapor interface, especially chemical reactions that are first catalyzed by the species at the surface. The nature and structure of the IL interface is also important for understanding the transport of chemical species across such interfaces.

For ILs, it was found both from simulations<sup>18–21</sup> and from experiments<sup>22,23</sup> that the local environment around the IL ions is highly anisotropic. For such a system, the ions may not be described well as rigid bodies, because their electron densities are distorted during the interactions with each other, making it highly desirable to model these interactions using a fully electronically polarizable force field.<sup>24</sup> Also, at the interfacial region, the three-dimensional (3D) symmetry of the interaction in the bulk region is broken, and it is important to have a polarizable model for investigating the ionic behavior at the interface, given the high polarizability of the IL ions.<sup>25,26</sup> In this study, we report MD simulations on the IL–vacuum interface to provide a clearer picture of the IL interface structural properties. In our previous study,<sup>26</sup> we developed a polarizable model for the ionic liquid 1-ethyl-3-methylimidazolium nitrate (EMIM<sup>+</sup>/NO<sub>3</sub><sup>−</sup>) and performed MD simulations of its bulk properties. In this study, we utilize the same methodology for defining the polarizable model, based on Thole’s smearing dipole technique,<sup>27,28</sup> but with a newly fitted set of anisotropic atomic polarizabilities. We then perform IL–vacuum interface MD simulation based on both the polarizable and nonpolarizable models.

The sections of this paper are organized as follows. In section II, the simulation methodology and model are described, while in section III, the results from the simulations are given and discussed. Section IV provides a summary and concluding remarks.

## II. Simulation Methodology and Model

The force field of the nonpolarizable IL model takes the standard form

$$V_{\text{nonpolar}} = \sum_{\text{bonds}} k_b(r - r_0)^2 + \sum_{\text{angles}} k_\theta(\theta - \theta_0)^2 + \sum_{\text{dihedrals}} V_n \cos(n\phi - \gamma) + \sum_i \sum_{j>i} \left( \frac{a_{ij}}{r_{ij}^{12}} + \frac{b_{ij}}{r_{ij}^6} + \frac{q_i q_j}{r_{ij}} \right) \quad (1)$$

where the force field parameters are described in our previous paper.<sup>20,26</sup> The partial charges of both EMIM<sup>+</sup> and NO<sub>3</sub><sup>−</sup> were fit to ab initio electrostatic potential (ESP) with the RESP fitting package.<sup>29</sup> The ab initio calculations were performed with Gaussian 03.<sup>30</sup> For EMIM<sup>+</sup>, the ESP grids were generated by MP2/6-31G(d) and fit to three configurations, i.e., (1) the MP2/6-31G(d)-optimized geometry, (2) the trans configuration, and (3) the cis configuration, while the partial charges were fit to the MP2/6-31G(d)-optimized structure for NO<sub>3</sub><sup>−</sup>. The potential given in eq 1 represents the nonpolarizable model in this work.

The RESP partial charges are valid for both nonpolarizable and polarizable force field models. For an isolated gas-phase ion with zero external fields, as performed in the ESP calculation, the induced dipole  $\mu_{\text{mol}}$  is zero and the distributed point partial charges represent the charge cloud as well as the permanent dipole uniquely. The dipole  $\mu_{\text{mol}}$  is induced only when an external electric field, or reaction field generated by other ions, is switched on. In the implementation of the polarizable force field, the intramolecular charge–dipole interactions are completely ignored, as a direct implementation of the interactive atomic dipole model,<sup>27,31</sup> i.e., there is no “self-induced dipole” within the same molecule in the absence of an external electric field. Therefore, for an isolated ion without an external field, both the nonpolarizable model and the polarizable model are equivalent to each other. Once the electric field is switched on through the intermolecular interactions, the polarizable model represents the deformation of the charge cloud of the ion in a more physically accurate manner. According to the interactive atomic dipole model,<sup>27,31</sup> all of the intramolecular dipole–dipole interactions are needed to rebuild a realistic anisotropic molecular dipole from the isotropic atomic dipoles.

The force field for the polarizable model is given by

$$V_{\text{polar}} = V_{\text{nonpolar}} - \sum_i \mu_i \cdot \mathbf{E}_i^0 - \sum_i \sum_{j>i} \mu_i \mu_j \cdot \mathbf{T}_{ij} + \sum_i \frac{\mu_i \cdot \mu_i}{2\alpha_i^2} \quad (2)$$

where the first term is given by eq 1, the second term represents charge–dipole interactions, the third term represents dipole–dipole interactions, and the last term is the energy required to induce the dipole. In eq 2,  $\mu_i$  and  $\mu_j$  represent the induced atomic dipole on atoms  $i$  and  $j$ , respectively,  $\mathbf{E}_i^0 = \sum_{j \neq i} q_j \mathbf{r}_{ij} / r_{ij}^3$  is the electric field on atom  $i$ , which is generated by the partial charges of all of the other atoms except the intramolecular atoms within the same ion, and  $\mathbf{T}_{ij}$  is the dipole field tensor between atoms  $i$  and  $j$ , which takes the following form

$$\mathbf{T}_{ij} = \begin{cases} \left( \frac{3\mathbf{r}_{ij}\mathbf{r}_{ij}}{r_{ij}^5} - \frac{\mathbf{I}}{r_{ij}^3} \right) - \left[ \frac{3\mathbf{r}_{ij}\mathbf{r}_{ij}}{r_{ij}^5} \exp\left(-\frac{A_{ij}}{r_{ij}}\right) \sum_{n=0}^3 \frac{1}{n!} \left(\frac{A_{ij}}{r_{ij}}\right)^n - \frac{\mathbf{I}}{r_{ij}^3} \exp\left(-\frac{A_{ij}}{r_{ij}}\right) \sum_{n=0}^2 \frac{1}{n!} \left(\frac{A_{ij}}{r_{ij}}\right)^n \right] & \text{for } i, j \text{ connected by intramolecular bond, angle, or dihedral terms} \\ \frac{3\mathbf{r}_{ij}\mathbf{r}_{ij}}{r_{ij}^5} - \frac{\mathbf{I}}{r_{ij}^3} & \text{otherwise} \end{cases} \quad (3)$$

where  $A_{ij} = (\alpha_i \alpha_j)^{1/6}$ .

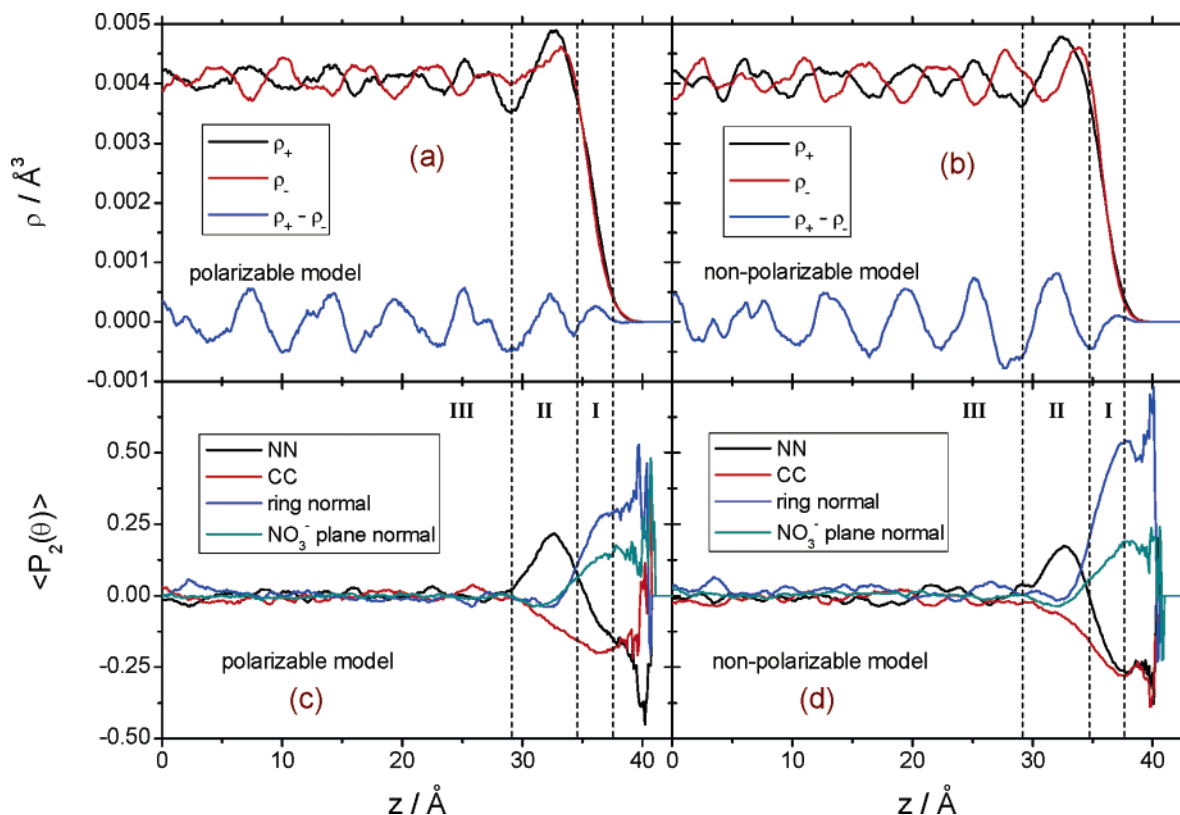


**Figure 2.** Number density profile and orientational ordering parameter of the EMIM<sup>+</sup> and NO<sub>3</sub><sup>−</sup> ions, for both the polarizable model (a and c) and the nonpolarizable model (b and d). In the top two plots, black denotes the density profile of EMIM<sup>+</sup>, red the density profile of NO<sub>3</sub><sup>−</sup>, and blue the difference in the density profiles between EMIM<sup>+</sup> and NO<sub>3</sub><sup>−</sup>. In the bottom two plots,  $\theta$  is defined by the angle between the direction vectors and the surface normal: black for the NN vector on EMIM<sup>+</sup>, red for the CC vector on EMIM<sup>+</sup>, blue for the imidazolium ring normal vector on EMIM<sup>+</sup>, and cyan for the plane normal vector on NO<sub>3</sub><sup>−</sup>. The regions enclosed by the vertical dashed lines are (I) the 10–90 region, (II) the dense region, and (III) the bulk region (see the text).

The atomic polarizability  $\alpha_i$  on the  $i$ th atom was fit to the ab initio molecular polarizability with MP2/aug-cc-pVDZ, in contrast to the MP2/cc-pVTZ(−f) level of theory in our previous study,<sup>26</sup> by adopting Thole's smeared atomic dipole model with smearing function  $\rho(r_{ij}) = (a^3/8\pi) \exp(-ar_{ij}/A_{ij})$ .<sup>27</sup> Specifically, the resulting atomic polarizabilities for EMIM<sup>+</sup> are 0.289 Å<sup>3</sup> for H, 1.209 Å<sup>3</sup> for C, and 0.680 Å<sup>3</sup> for N, while for NO<sub>3</sub><sup>−</sup>, they are 1.901 Å<sup>3</sup> for N and 1.079 Å<sup>3</sup> for O, with the Thole smearing factor  $a$  equal to 2.392. Details of the polarizable IL model will be reported later,<sup>32</sup> but here we note that the current fits give accurate anisotropic molecular polarizabilities against an ab initio MP2/aug-cc-pVDZ level of theory. In particular, at the MP2/6-31g\*-optimized geometry, we obtain values of 11.75 Å<sup>3</sup> for EMIM<sup>+</sup> and 4.86 Å<sup>3</sup> for NO<sub>3</sub><sup>−</sup>, from the above fitted atomic polarizabilities, compared to the MP2/aug-cc-pVDZ values of 11.71 Å<sup>3</sup> for EMIM<sup>+</sup> and 4.86 Å<sup>3</sup> for NO<sub>3</sub><sup>−</sup>. The induced dipole on atom  $i$  is  $\mu_i = \alpha_i(\mathbf{E}_i^0 + \sum_{j \neq i} \mathbf{T}_{ij}\mu_j)$ . Equation 2, with the Ewald sum for the long-range charge–charge, charge–dipole, and dipole–dipole interactions,<sup>33</sup> was implemented in DL\_POLY 2.13<sup>34</sup> and parallelized with the replicated data method.<sup>35</sup>

For both nonpolarizable and polarizable models, the IL system consists of 600 ionic liquid 1-ethyl-3-methylimidazolium nitrate (EMIM<sup>+</sup>/NO<sub>3</sub><sup>−</sup>) ion pairs (13 800 atoms) in an all-atom, all-flexible model. The periodic boundary condition was employed with a rectangular cell of 45 Å × 45 Å × 135 Å. The surface normal direction was elongated (135 Å) so the ionic liquid slab occupies ~80 Å in the middle with two equivalent interfaces. The results were then averaged over these two interfaces, and the positive side of the slab is shown in the figures. Figure 1

shows the various direction vectors of EMIM<sup>+</sup> used in the analysis of the trajectory results.

The system was coupled to a Nosé-Hoover thermostat (constant NVT)<sup>36,37</sup> at 400 K. For the polarizable model, the induced dipole was propagated by an extended Lagrangian<sup>38</sup> and coupled to another Nosé-Hoover thermostat<sup>36,37</sup> at 0.1 K to keep it evolving on the adiabatic surface.<sup>39</sup> The integration time step was 0.45 fs for the polarizable model and 1 fs for the nonpolarizable model. After a 1 ns constant NVT equilibration at 400 K, the MD production runs were 2.2 ns for the polarizable model and 3.2 ns for the nonpolarizable model, with phase space data (velocities and coordinates) recorded every 4.5 fs for the polarizable model and every 5 fs for the nonpolarizable model. No detectable vapor phase was observed during the simulation. Because of the large amount of phase space data, the error bars are quite small and not shown in the figures. However, it is always possible for such strongly interacting systems to be trapped in a local minimum in the phase space for a relatively long time.<sup>5,40</sup>

### III. Results and Discussion

**A. Density Profile and Orientational Ordering.** Panels a and b of Figure 2 show the center-of-mass number density profile for the polarizable model and the nonpolarizable model, respectively. The strong oscillation seen in the density profile, which extends to more than 40 Å, indicates a supercooled liquid behavior as discussed in our previous study,<sup>20</sup> though the simulations were run at 400 K, which is much higher than the experimental melting point of ~311 K. Another feature seen from the density profiles is that there exists a dense region, in



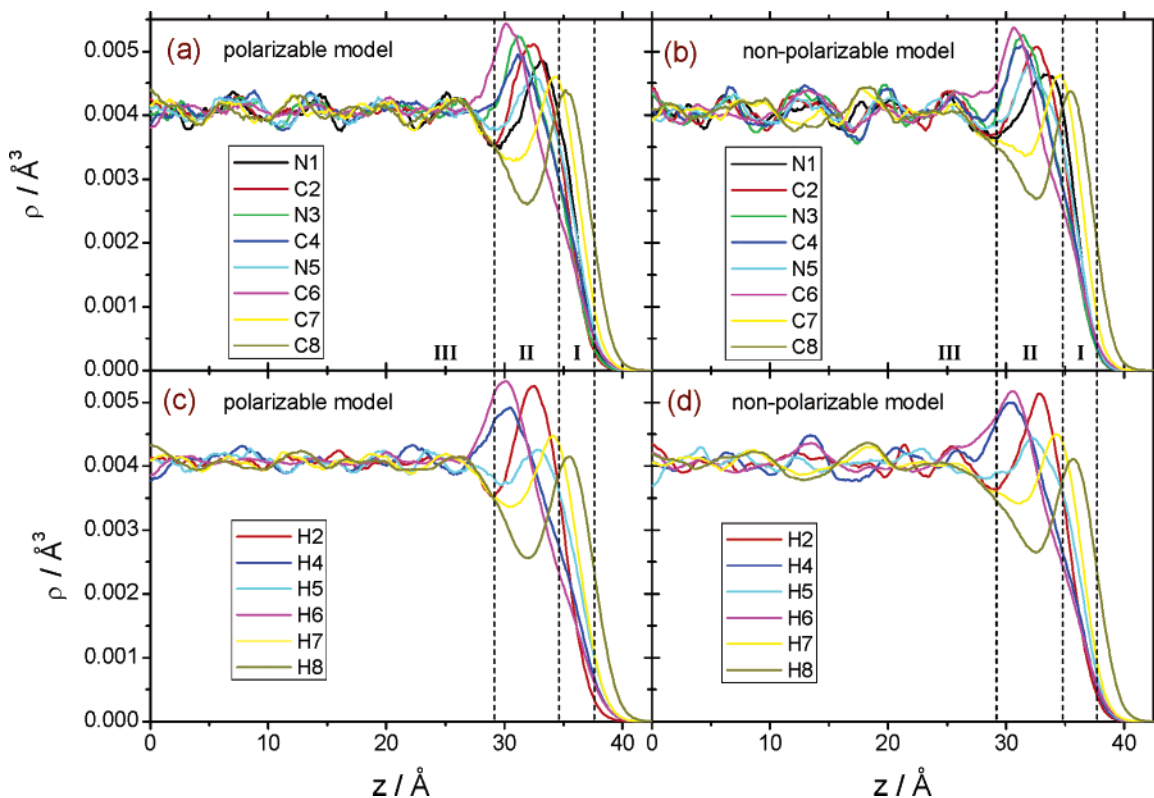


**Figure 3.** Number density profile of individual atoms, where the atomic indexing is in accord with Figure 1. For the hydrogen atoms, the indistinguishable H6, H7, and H8 atoms are weighted by 3, 2, and 3, respectively, for better comparison. The regions enclosed by the vertical dashed lines, i.e., (I) the 10–90 region, (II) the dense region, and (III) the bulk region, are the same as in Figure 2.

which the ionic density is higher than the bulk density, especially for the cation. Motivated by the above observation, we divided the simulation slab into three regions: (I) the 10–90 region, in which the cationic density varies from 10 to 90% of the average bulk density; (II) the dense region, which starts from the end of the 10–90 region and extends to the first minimum of the first cationic density oscillation; and (III) the bulk region, which starts from the end of the dense region and extends to the inner liquid bulk.

Panels c and d of Figure 2 show the orientational ordering parameters, defined as the average of the second Legendre polynomial

$$\langle P_2(\theta) \rangle = \left\langle \frac{1}{2}(3 \cos^2 \theta - 1) \right\rangle \quad (4)$$

for both the polarizable model and the nonpolarizable model. In eq 4,  $\theta$  is taken as the angle between a specific direction vector (see Figure 1) and the surface normal  $z$ . It can be seen that in the 10–90 region both the cation and anion show a tendency to lie on the surface with the imidazolium ring normal on EMIM<sup>+</sup> and the NO<sub>3</sub><sup>−</sup> plane normal in alignment with the surface normal. The NN vector and the CC vector on EMIM<sup>+</sup> also show a tendency to be perpendicular to the surface normal. In the region where ionic liquid density is less than 10% of the bulk density, this trend becomes even more pronounced, although the statistics become poor in that region. The NN vector's preferred direction changes gradually from the 10–90 region to the dense region, and in the latter, it becomes likely to be in alignment with the surface normal while the EMIM<sup>+</sup> ring normal direction and the NO<sub>3</sub><sup>−</sup> plane normal direction are randomized and slightly prefer to be perpendicular to the surface normal. In the bulk region, all of the vectors become randomized.

Figure 3 shows the number density profile of the individual heavy atoms as well as the indistinguishable hydrogen atom groups on the EMIM<sup>+</sup> (see Figure 1). The definitions of the three regions are the same as in Figure 2. It can be seen that C8 and H8 are consistently the outermost ones and the C6 and H6 atoms are consistently the innermost ones. Also, deep minima for C8 and H8 occur in the dense region. Such features are seen for both the polarizable and nonpolarizable models. Thus, at the interfacial region, EMIM<sup>+</sup> has a strong tendency to slant with the long chain methyl side group protruding outward from the surface and the short chain methyl side group pointing inward from the surface. The segregation of atoms at the interface is also evident from Figure 3, because of the alignment of the ions near the surface. The 10–90 region and the dense region altogether contain approximately one to two layers of EMIM<sup>+</sup>. Further analyses of the angular distributions of the angle  $\theta$  between the direction vectors and the surface normal, for the three individual regions, show the same trend (see the Supporting Information).

**B. Lateral Interface Structure.** To further investigate the lateral interfacial structure, the tangential radial distribution function (TRDF) was computed<sup>41</sup>

$$g(r) = \frac{\sum_{ij} \delta(r - r_{ij})}{2\pi r \, dr \, \rho^{\text{region}} \Delta z}; \quad z_{ij} < \Delta z \text{ and } r_{ij} = \sqrt{x_{ij}^2 + y_{ij}^2} \quad (5)$$

where  $\Delta z = 1 \text{ Å}$ ,  $\rho^{\text{region}}$  is the average number density in each region which normalizes the TRDF of each region to unity at infinite distance  $r_{ij}$ , and  $r_{ij}$  is the two-dimensional center-of-mass distance parallel to the surface plane between the  $i$ th and  $j$ th ion.

Figure 4 shows the cation–cation, anion–anion, and cation–anion TRDF in the 10–90 region, the dense region, and the

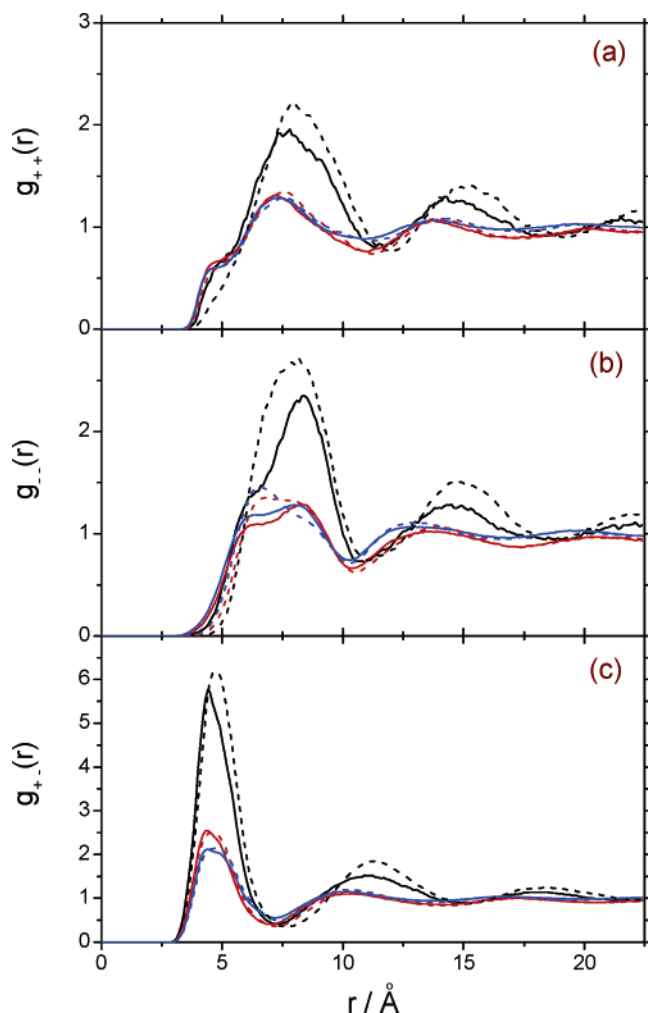


**Figure 4.** Tangential radial distribution function (TRDF) of individual regions for both the polarizable model and the nonpolarizable model: (a)  $g_{++}(r)$ , (b)  $g_{--}(r)$ , and (c)  $g_{+-}(r)$ . Black denotes the 10–90 region, red the dense region, blue the bulk region, the solid line the polarizable model, and the dashed line the nonpolarizable model.

bulk region, for both the polarizable model and the nonpolarizable model, respectively. It can be seen that in the 10–90 region, a higher first peak is observed than in the other two regions. The oscillation of the TRDF in the 10–90 region is also more pronounced. Since the average number density of the 10–90 region is much lower than that of the dense region or the bulk region, the high first peak demonstrates that local clusters, in which each ion tends to keep a coordination number similar to that of the bulk, is formed in this dilute region.<sup>41</sup> Thus, a surface corrugation is reflected in the TRDF in the 10–90 region, in which the oscillation is the most intense, and such a feature is present in both the polarizable model and the nonpolarizable model.

Figure 5 shows two individual snapshots, one from the polarizable model and one from the nonpolarizable model, taken from the MD simulation, in which the outermost 20 cation–anion pairs are shown as space filling models on the background of the deeper layers, shown as stick models. Since the snapshots were taken randomly, they may or may not be representative of the major structural properties. However, since this system is mainly governed by the electrostatic interactions with relatively slow dynamics, the snapshot should retain its configuration for a relatively long time. It can be seen from the two snapshots that for both the polarizable and the nonpolarizable model there are laterally oriented clusters as well as voids

formed in the interfacial region. Thus, the distribution of the ions on the surface is far from even, with the ionic liquid–vacuum interfacial region being highly corrugated.

It is also noticeable that the “bump” at  $\sim 4.5$  Å in the  $g_{++}(r)$  plot in Figure 4a is less pronounced in the 10–90 region, especially for the nonpolarizable model, but is slightly more intense in the dense region than that in the bulk region. The experimental crystal structure of EMIM<sup>+</sup>/NO<sub>3</sub><sup>−</sup> shows that the ions are nearly parallel with the interplanar separation of the ions at 4.5 Å.<sup>42</sup> Therefore, the bump observed in the  $g_{++}(r)$  plot may be attributed to this crystal structure feature, for which the cations are closely packed to give the higher bump in the dense region. As Lynden-Bell pointed out,<sup>4</sup> the cation in this region is likely to align with the imidazolium ring plane perpendicular to the surface so that the density is enhanced in the dense region.

**C. Difference between Polarizable and Nonpolarizable Models.** In Figure 2, both the polarizable model and the nonpolarizable model show an alternating cation–anion surface-normal density oscillation and thus a surface-normal charge density oscillation. The computer simulations of Lynden-Bell<sup>4,5</sup> for the IL DMIM<sup>+</sup>/Cl<sup>−</sup> also yielded a layered surface with an oscillatory density profile. However, the charge oscillation shown in Figure 2 is more enhanced near the surface for the nonpolarizable model than for the polarizable model. This may be attributed to the polarization effect, which helps to balance the charge density difference by the induced dipole on the surface for the polarizable model. It can also be seen from the TRDF in Figure 4 that the ions are in closer contact for the polarizable model than for the nonpolarizable model. The induced dipole screens the charge–charge repulsion in  $g_{++}(r)$  and  $g_{--}(r)$ , while it screens the short-range repulsion in  $g_{+-}(r)$ . Also, the first peaks in  $g_{++}(r)$  and  $g_{+-}(r)$  plots occur at shorter distances for the polarizable model, while that in the  $g_{--}(r)$  plot occurs at longer distances.

A further analysis of the short-distance arrangement for NO<sub>3</sub><sup>−</sup> around a central NO<sub>3</sub><sup>−</sup> shows a quite different packing pattern for the two models. For the polarizable model, NO<sub>3</sub><sup>−</sup> is most likely to pack on the O–N–O edge region around the central NO<sub>3</sub><sup>−</sup>. For the nonpolarizable model, the NO<sub>3</sub><sup>−</sup> is most likely to pack around the O atom vertex of the central NO<sub>3</sub><sup>−</sup>.<sup>32</sup> The difference in the most likely anion–anion packing pattern for the two models gives different first maxima in  $g_{--}(r)$ , as shown in Figure 4b, which can be seen clearly in the bulk region. Briefly, this may again be explained by the polarization effect. Since the polarizability of NO<sub>3</sub><sup>−</sup> is approximately one-third of that of EMIM<sup>+</sup>, the spatial arrangement of the NO<sub>3</sub><sup>−</sup> seems to help in maximizing the local electric field on EMIM<sup>+</sup>. Thus, the difference seen in the TRDFs may be explained by the polarization effect, as in our previous study.<sup>26</sup>

The surface tension is given by

$$\gamma = \frac{L_z}{2} \left( \langle \Pi_{zz} \rangle - \frac{1}{2} \langle \Pi_{xx} + \Pi_{yy} \rangle \right) \quad (6)$$

where  $\Pi_{xx}$ ,  $\Pi_{yy}$ , and  $\Pi_{zz}$  are the principal components of the pressure tensor,  $L_z$  ( $=135$  Å) is the length of the PBC box along the surface normal, and  $L_z/2$  comes from the fact that there are two equivalent interfaces in the simulation. Figure 6 shows the running average of the surface tension of the polarizable and nonpolarizable models.

According to the experimental surface tension results of Law and Watson,<sup>7</sup> for C<sub>n</sub>mim<sup>+</sup> ILs containing the same anion, the surface tension diminishes with increasing alkyl chain length and it spans an unusually wide range for different side chain



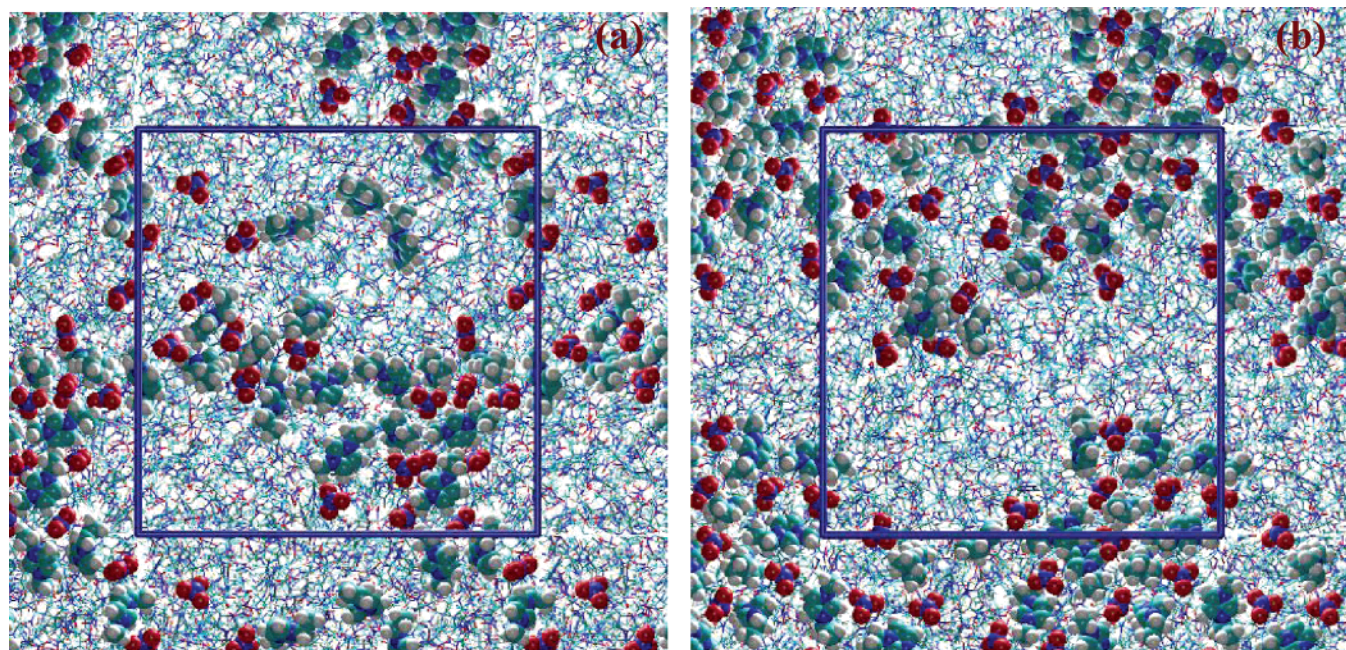


**Figure 5.** Two snapshots taken randomly near the end of the MD production run: (a) polarizable model and (b) nonpolarizable model. The configurations are shown via top views, and the square box shows the periodic system of  $45 \text{ \AA} \times 45 \text{ \AA}$ , outside which are the periodic images for a better view. The outermost surface layer ions are shown as space filling models, while in the background, the stick model is used for the ions in the deeper layers.

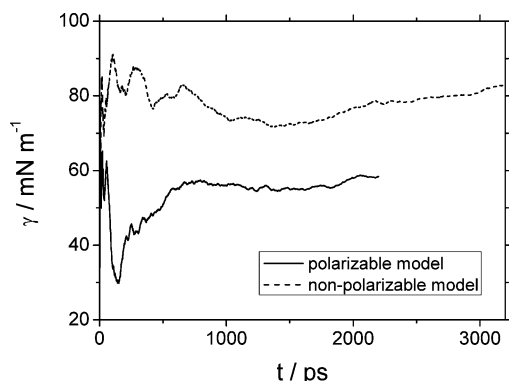


**Figure 6.** Running average of the surface tension for both the polarizable model (solid line) and the nonpolarizable model (dashed line).

lengths. Likewise, for a fixed cation, in general, the compound with the larger anion has the higher surface tension,<sup>7,16</sup> but the surface tensions span a narrow range. Considering the special size of  $\text{NO}_3^-$  compared to those of  $\text{PF}_6^-$ ,  $\text{BF}_4^-$ ,  $\text{Cl}^-$ , and  $\text{I}^-$ , we estimate that the surface tension of  $\text{EMIM}^+/\text{NO}_3^-$  is  $\sim 40\text{--}50 \text{ mN/m}^2$  at 400 K by extrapolating the existing values from Table 2 of ref 7. Considering the finite size effect in the interfacial simulation,<sup>43,44</sup> the surface tension of the polarizable model is quite reasonable, while that of the nonpolarizable model is too high. By the end of the MD production run, the surface tension was found to be  $58.5 \pm 0.5 \text{ mN/m}$  for the polarizable model and  $82.7 \pm 0.6 \text{ mN/m}$  for the nonpolarizable model, with

a 95% confidence interval. Therefore, the polarizable model gives a surface tension in better agreement with the extrapolated experimental surface tension. This is in agreement with our previous bulk simulations,<sup>26</sup> in which we showed that the polarizable model is more mobile, with a higher self-diffusion coefficient and lower viscosity, than the nonpolarizable model.

Finally, Table 1 shows the average number density in each region. It can be seen that the cation of the polarizable model tends to be segregated into the 10–90 region. By contrast, the anion of the nonpolarizable model tends to be segregated into the 10–90 region. Apparently, the polarization effect is important at the interfacial region for the surface segregation of the ions. Madden and co-workers, in their simulation of inorganic molten salts, found that the access of the polarizable ion to the surface will create the induced dipole moment to balance the displacement dipole moment and thus is electrostatically favorable.<sup>45</sup> Furthermore, only with a polarizable model was the anion (i.e., the ion with larger polarizability) found to be segregated to the surface, while no surface access was observed in a nonpolarizable inorganic molten salt model.<sup>45</sup> Similar results of surface access due to the polarization effect have also been observed in other computational studies of the liquid–vapor interface.<sup>46</sup>

In this study, the polarizability of  $\text{EMIM}^+$  is  $\sim 3$  times that of  $\text{NO}_3^-$ . Therefore, it is reasonable to see the segregation of the cation to the 10–90 region for the polarizable model. For the nonpolarizable model, since the cation is quite bulky with the ethyl side group protruding outward from the surface in the

**TABLE 1: Average Number Density<sup>a</sup> in Each Region and Segregation Ratio**

region <sup>b</sup>	polarizable			nonpolarizable		
	$\rho_{\text{cation}} (\times 10^3 \text{ \AA}^3)$	$\rho_{\text{anion}} (\times 10^3 \text{ \AA}^3)$	$(\rho_{\text{cation}} - \rho_{\text{anion}})/\rho_{\text{cation}} (\%)$	$\rho_{\text{cation}} (\times 10^3 \text{ \AA}^3)$	$\rho_{\text{anion}} (10^3 \text{ \AA}^3)$	$(\rho_{\text{cation}} - \rho_{\text{anion}})/\rho_{\text{cation}} (\%)$
10–90	$2.106 \pm 0.037$	$1.974 \pm 0.037$	$6.3 \pm 3.5$	$1.826 \pm 0.035$	$1.921 \pm 0.036$	$-5.2 \pm 4.0$
dense	$4.403 \pm 0.027$	$4.413 \pm 0.026$	$-0.2 \pm 1.2$	$4.405 \pm 0.026$	$4.238 \pm 0.019$	$3.8 \pm 1.0$
bulk <sup>c</sup>	$4.036 \pm 0.004$	$4.048 \pm 0.004$	$-0.3 \pm 0.2$	$4.043 \pm 0.004$	$4.066 \pm 0.003$	$-0.6 \pm 0.2$

<sup>a</sup> Errors with a 95% confidence interval. <sup>b</sup> See part A of section III for the definition of different regions in this study. <sup>c</sup> For an infinite system, the  $(\rho_{\text{cation}} - \rho_{\text{anion}})/\rho_{\text{cation}}$  ratio in the bulk region should be zero.

10–90 region, it is energetically favorable to have more counterions in this region to balance the charge. Thus, a stronger center-of-mass charge layering structure was observed for the nonpolarizable model.

#### IV. Summary and Concluding Remarks

In this paper, molecular dynamics simulations of the IL–vacuum interface have been carried out for a polarizable model and a nonpolarizable model. It is seen that the charge density at the interface for the polarizable model is reduced relative to that of the nonpolarizable model. The polarizable model also brings the ions into closer contact by screening their repulsion. The surface tension of the polarizable model is also significantly lower than that for the nonpolarizable model, the former being in better agreement with the experimental value and with simulations of polarizable molten salts.<sup>41</sup> A surface excess of the cation is found for the polarizable model, in contrast to a surface excess of the anion for the nonpolarizable model.

The major structural properties for both models are, however, found to be similar, for example, the oscillation in the number density profile, the preferred orientational ordering in the 10–90 region and the dense region, and the local lateral clustering at the interface. The EMIM<sup>+</sup> cation has a tendency to lie on the surface with the imidazolium ring parallel to the interface, in agreement with experimental sum frequency generation (SFG) spectroscopy.<sup>10,11</sup> There also exists a dense region near the surface, as reported previously in both experiments<sup>13,16</sup> and computer simulations.<sup>4,5</sup> In the dense region, EMIM<sup>+</sup> is likely to slant to form a lamellar structure, in agreement with the experimental neutron reflectometry (NR) measurements.<sup>13</sup> It is also found that the ethyl side group, with the longer alkane chain, has a tendency to protrude outward from the surface. The properties described in this paragraph are shared by both the polarizable and nonpolarizable models, and they are largely in agreement with the results of Lynden-Bell for a rigid 10-site, united-methyl group, DMIM<sup>+</sup>/Cl<sup>−</sup> nonpolarizable model.<sup>4</sup> In a future paper, a coarse-grained IL model will be utilized to simulate the ionic liquid interface over much larger length and time scales.

**Acknowledgment.** This research was supported by Air Force Office of Scientific Research (FA9550-04-1-0381) and partly supported by the 973 Program (2002CB211800) of China, the NKstars HPC program, and Renshi Chu startup funding of Nankai University. The allocations of supercomputing time at the Center for High Performance Computing (CHPC) at the University of Utah and the Institute of Scientific Computing at Nankai University are gratefully acknowledged.

**Supporting Information Available:** Angular distribution of  $\theta$  between direction vectors and the surface normal (Figure SI). This material is available free of charge via the Internet at <http://pubs.acs.org>.

#### References and Notes

- (1) Welton, T. *Chem. Rev.* **1999**, 99, 2071.
- (2) Wasserscheid, P.; Keim, W. *Angew. Chem., Int. Ed.* **2000**, 39, 3772.
- (3) Rogers, R. D.; Seddon, K. R. *Science* **2003**, 302, 792.
- (4) Lynden-Bell, R. M. *Mol. Phys.* **2003**, 101, 2625.
- (5) Lynden-Bell, R. M.; Kohanoff, J.; Del Pópolo, M. G. *Faraday Discuss.* **2005**, 129, 57.
- (6) Gannon, T. J.; Law, G.; Watson, P. R. *Langmuir* **1999**, 15, 8429.
- (7) Law, G.; Watson, P. R. *Langmuir* **2001**, 17, 6138.
- (8) Law, G.; Watson, P. R. *Chem. Phys. Lett.* **2001**, 345, 1.
- (9) Law, G.; Watson, P. R.; Carmichael, A. J.; Seddon, K. R. *Phys. Chem. Chem. Phys.* **2001**, 3, 2879.
- (10) Baldelli, S. *J. Phys. Chem. B* **2003**, 107, 6148.
- (11) Rivera-Rubero, S.; Baldelli, S. *J. Am. Chem. Soc.* **2004**, 126, 11788.
- (12) Fletcher, K. A.; Pandey, S. *Langmuir* **2004**, 20, 33.
- (13) Bowers, J.; Vergara-Gutierrez, M. C. *Langmuir* **2004**, 20, 309.
- (14) Bowers, J.; Butts, C. P.; Martin, P. J.; Vergara-Gutierrez, M. C.; Heenan, R. K. *Langmuir* **2004**, 20, 2191.
- (15) Iimori, T.; Iwahashi, T.; Ishii, H.; Seki, K.; Ouchi, Y.; Ozawa, R.; Hamaguchi, H.; Kim, D. *Chem. Phys. Lett.* **2004**, 389, 321.
- (16) Solutskin, E.; Ocko, B. M.; Taman, L.; Kuzmenko, I.; Gog, T.; Deutsch, M. *J. Am. Chem. Soc.* **2005**, 127, 7796.
- (17) Halka, V.; Tsekov, R.; Freyland, W. *Phys. Chem. Chem. Phys.* **2005**, 7, 2038.
- (18) Hanke, C. G.; Price, S. L.; Lynden-Bell, R. M. *Mol. Phys.* **2001**, 99, 801.
- (19) Margulis, C. J.; Stern, H. A.; Berne, B. J. *J. Phys. Chem. B* **2002**, 106, 12017.
- (20) Del Pópolo, M. G.; Voth, G. A. *J. Phys. Chem. B* **2004**, 108, 1744.
- (21) Urahata, S. M.; Ribeiro, M. C. C. *J. Chem. Phys.* **2004**, 120, 1855.
- (22) Hardacre, C.; Holbrey, J. D.; Jane McMath, S. E.; Bowron, D. T.; Soper, A. K. *J. Chem. Phys.* **2003**, 118, 273.
- (23) Hardacre, C.; Jane McMath, S. E.; Nieuwenhuyzen, M.; Bowron, D. T.; Soper, A. K. *J. Phys.: Condens. Matter* **2003**, 15, S159.
- (24) Gray-Weale, A.; Madden, P. A. *Mol. Phys.* **2003**, 101, 1761.
- (25) Cang, H.; Li, J.; Fayer, M. D. *J. Chem. Phys.* **2003**, 119, 13017.
- (26) Yan, T.; Burnham, C. J.; Del Pópolo, M. G.; Voth, G. A. *J. Phys. Chem. B* **2004**, 108, 11877.
- (27) Thole, B. T. *Chem. Phys.* **1981**, 59, 341.
- (28) Burnham, C. J.; Li, J.; Xantheas, S. S. *J. Chem. Phys.* **1999**, 110, 4566.
- (29) Cornell, W. D.; Cieplak, P.; Bayly, C. I.; Kollman, P. A. *J. Am. Chem. Soc.* **1993**, 115, 9620.
- (30) Frisch, M. J.; Trucks, G. W.; Schlegel, H. B.; et al. *Gaussian 03*, version B02; Gaussian, Inc.: Pittsburgh, PA, 2003.
- (31) Applequist, J.; Carl, J. R.; Fung, K.-K. *J. Am. Chem. Soc.* **1972**, 94, 2952.
- (32) Yan, T.; Burnham, C. J.; Wang, Y. T.; Gao, X. P.; Voth, G. A. Manuscript in preparation.
- (33) Smith, W. *CCP5 Information Quarterly* **1982**, 4, 13.
- (34) Smith, W.; Forester, T. R. *The DL\_POLY Molecular Simulation Package*; [http://www.dl.ac.uk/TCSC/Software/DL\\_POLY/main.html](http://www.dl.ac.uk/TCSC/Software/DL_POLY/main.html), 1999.
- (35) Smith, W. *Comput. Phys. Commun.* **1992**, 67, 392.
- (36) Nosé, S. *J. Chem. Phys.* **1984**, 81, 511.
- (37) Hoover, W. G. *Phys. Rev. A* **1985**, 31, 1695.
- (38) Saboungi, M.-L.; Rahman, A.; Halley, J. W.; Blander, M. *J. Chem. Phys.* **1988**, 88, 5818.
- (39) Sprik, M. *J. Phys. Chem.* **1991**, 95, 2283.
- (40) Venkatnathan, A.; Voth, G. A. *J. Chem. Theory Comput.* **2005**, 1, 36.
- (41) Aguado, A.; Wilson, M.; Madden, P. A. *J. Chem. Phys.* **2001**, 115, 8603.
- (42) Wilkes, J. S.; Zaworotko, M. J. *J. Chem. Soc., Chem. Commun.* **1992**, 965.
- (43) Aguado, A.; Scott, W.; Madden, P. A. *J. Chem. Phys.* **2001**, 115, 8612.
- (44) González-Melchor, M.; Bresme, F.; Alejandre, J. *J. Chem. Phys.* **2005**, 122, 104710.
- (45) Aguado, A.; Madden, P. A. *J. Chem. Phys.* **2002**, 117, 7659.
- (46) Mucha, M.; Frigato, T.; Levering, L. M.; Allen, H. C.; Tobias, D. J.; Dang, L. X.; Jungwirth, P. *J. Phys. Chem. B* **2005**, 109, 7617.